PHYSICAL REVIEW B **107**, 165120 (2023)

Non-Hermitian higher-order Weyl semimetal with surface diabolic points

Subhajyoti Bid, Gaurab Kumar Dash, and Manisha Thakurathi
Department of Physics, Indian Institute of Technology Delhi, Hauz Khas, New Delhi 110016, India

(Received 3 January 2023; revised 31 January 2023; accepted 24 March 2023; published 10 April 2023)

Higher-order topology in non-Hermitian (NH) systems has recently become one of the most promising and rapidly developing fields in condensed-matter physics. Many distinct phases that were not present in the Hermitian equivalents are revealed in these systems. In this work, we examine how higher-order Weyl semimetals are impacted by NH perturbation. We identify a new type of topological semimetal, i.e., non-Hermitian higher-order Weyl semimetal (NHHOWS) with surface diabolic points. We demonstrate that in such an NHHOWS, new exceptional points inside the bulk can be created and annihilated, therefore allowing us to manipulate their number. At the boundary, these exceptional points are connected through unique surface states with diabolic points and hinge states. For specific system parameters, the surface of NHHOWS behaves as a Dirac phase with linear dispersion or a Luttinger phase with a quadratic dispersion, thus paving a way for Dirac-Luttinger switching. Finally, we employ the biorthogonal technique to reinstate the standard bulk-boundary correspondence for NH systems and compute the topological invariants. The obtained quantized biorthogonal Chern number and quadruple moment topologically protect the unique surface and hinge states, respectively.

DOI: 10.1103/PhysRevB.107.165120

I. INTRODUCTION

Since the early 2010s, topological phases such as topological insulators [1–7], topological superconductors [8–17], and Dirac/Weyl semimetal [18–22] in Hermitian systems have been attracting substantial attention. Currently, the field of non-Hermitian (NH) topological systems [23–31] is also rapidly emerging with a variety of potential applications in condensed-matter physics. One of the key features of NH systems is the existence of a unique branch point in the spectrum, known as an exceptional point (EP), where both eigenenergies, as well as eigenvectors, coalesce. This is quite different from a conventional well-known degenerate point in Hermitian systems, named as diabolic point (DP), at which only the eigenenergies coalesce. Although DPs have a variety of characteristics, their physics in non-Hermitian systems is less explored. It has been observed generally that the DPs are not stable and split into EPs or evolve into exceptional rings in the presence of NH terms in the Hamiltonian [32,33].

In this work, we describe a method for generating DPs on the surface of an NH system while sustaining EPs in the bulk of the systems. We illustrate that the DPs change their location on the surface as well as dispersion around them when the system parameters vary. This allows us to achieve the Dirac to Luttinger phase switch on the surface. Notably, DPs emerge precisely at those locations in momenta where the Dirac nodes are formed in the higher-order Dirac semimetal (HODS) [26,34,35], thus retaining the memory of HODS phase. We begin with a C_4^z symmetric higher-order Weyl semimetal (HOWS) which is created by breaking the degeneracy of each Dirac node in HODS. We unravel the fate of such a system under NH Weyl perturbation (responsible for breaking the degeneracy of Dirac points) due to nonreciprocal couplings in the system. The NH perturbation in the Hamiltonian breaks each Weyl node into two EPs. Starting from eight we can decrease their number to six, four, two, and zero by annihilating them or vice versa by tuning the system parameters. Some of the EPs are connected either by bulk Fermi arcs (FA) [36] or surface FAs when the system is finite along one axis. Remarkably, the energy eigenvalues of the surface FAs, have degenerate DPs and a variety of dispersion spectra around them. For certain system parameters, we can achieve a Dirac phase having an absolute value of energy $\sim |k|$ as well as a Luttinger phase with k^2 dispersion relations. Since these EPs are connected by surface states so we identify them as normal-order EPs which are characterized by quantized open-boundary Chern number. When the system is finite along two directions, we find that the innermost EPs closest to the Γ point in Brillouin zone (BZ) are connected by hinge states, which are completely flat bands localized only at the hinges of the system. In recent literature, hinges are characterized by higher-order topology, and therefore the corresponding EPs connecting them are of higher order in nature [37,38]. Among many, one of the interesting feature of NH systems is the breaking down of bulk-boundary correspondence (BBC). This is due to the fact that these systems exhibit non-Hermitian skin effect [39–43]. To restore BBC, generally, two distinctive approaches are used: (i) generalized Brillouin zone approach [44] and (ii) biorthogonal real-space approach [45]. Due to the simplicity and convenience, we use the latter approach to calculate the topological invariants, namely open-boundary Chern number [45] and quadrupole moment [46,47], for unraveling the theory of normal as well as higher-order topological phase of this novel semimetal. Our theoretical proposal can readily be realized on topolectrical circuit lattices [48]. Consequently, it may be foundational for future experiments aimed at a controlled manipulation of Dirac to Luttinger dispersion.

The outline of the paper is as follows. In Sec. II, we discuss the model under consideration followed by the phase diagram

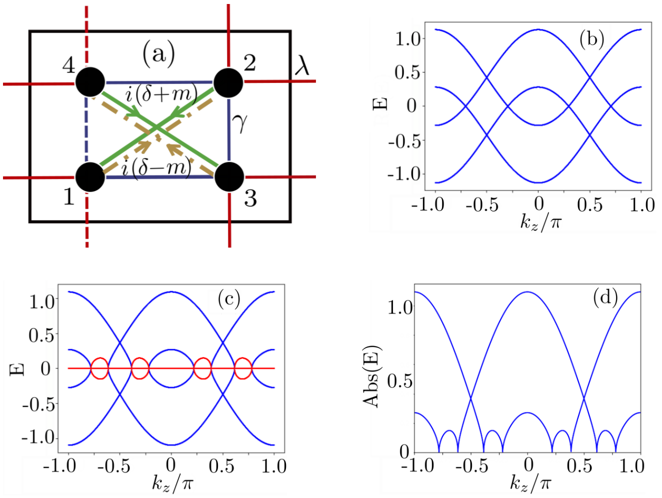

FIG. 1. (a) Schematic diagram of unit cell with intercell hopping as λ, nearest-neighbor intracell hopping as γ and NH next nearest-neighbor intracell hopping as $i(\delta \pm m)$. Dashed lines signify the opposite sign of hopping compared to solid ones. The bulk energy spectrum of (b) $H_0(k)$ with four DPs for $\gamma = -1$, $m = 0.6/\sqrt{2}$, and $\delta = 0$ and (c) for $H_{\rm NHW}(k)$ having eight EPs when $\delta = m/2$ with blue (red) representing the real (imaginary) part of energy eigenvalues. The non-Hermitian term, δ, creates new EPs in the system, and therefore the number of EPs changes as we vary the value of γ and δ. (d) Plot of the absolute energy as a function of k_z with eight EPs for the same system parameters.

analysis. In Sec. III, we study the surface and hinge states. Next, we compute the topological invariants in Sec. IV and different systems which preserve inversion and time-reversal symmetry have been considered in Secs. IV and V, respectively. We conclude in Sec. V. Technical details are deferred to four Appendixes.

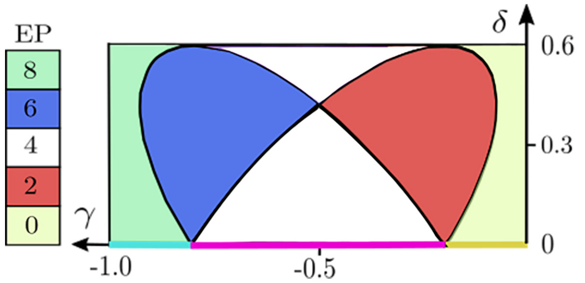

FIG. 2. The phase diagram for the number of EPs in the bulk with elliptical phase boundaries. From the extreme left ($\gamma = -1$) we start with eight EPs and gradually annihilate them to decrease their number. One cannot directly reach from eight to zero EPs. There exist an interesting point in the phase diagram with values $\gamma = -0.5$ and $\delta \sim 0.4$, which we name the triple point of EPs in the bulk. Infinitesimal change around this point marks a phase transition and takes us to phases with different number of EPs.

II. MODEL AND PHASE DIAGRAM

We consider HOWS, constructed by stacking two-dimensional (2D) quadrupole insulators along the z axis [26,47]. The Hamiltonian using spinless fermion has the form $H_{\rm NHW}(k) = H_0(k) + i\,\delta\sigma_0\kappa_1$, where $H_0(k)$ is the Hermitian part and is given by

$$H_0(k) = \sum_{j=1}^{4} h_j \Gamma_j + m\sigma_0\kappa_2. \qquad (1)$$

Here $h_{1/3} = \sin k_{y/x}$ and $h_{2/4} = (\gamma + 0.5\cos k_z + \cos k_{y/x})$. The intercell hopping is denoted by γ; the direct product of Pauli matrices have the form $\Gamma_0 = \sigma^3\kappa^0$, $\Gamma_i = -\sigma^2\kappa^i$, and $\Gamma_4 = \sigma^1\kappa^0$; and m is intracell coupling with δ added as the NH contribution to it as shown in Fig. 1(a). In Eq. (1), spinless time-reversal symmetry $\mathcal{T} = \mathcal{K}$, where $\mathcal{K}$ is complex conjugate, and mirror symmetries (M_x and M_y) are broken due to the m term. However, it preserves C_4^z, inversion ($\mathcal{P}$), $M_x\mathcal{T}$, and $M_y\mathcal{T}$. This term splits the Dirac nodes into two Weyl nodes with opposite monopole charges. It has been shown in Ref. [26] that at most four Weyl nodes of both first- and second-order connected via surface and hinge arcs, respectively, can be obtained. Furthermore, with the addition of the non-Hermitian coupling δ, multiple EPs emerge where both the real, as well as the complex, part of the energy goes to zero. The δ term preserves charge conjugation ($\mathcal{C}$) and $\mathcal{CP}$. However, it breaks symmetries like inversion ($\mathcal{P}$), C_4^z, $M_x\mathcal{T}$, $M_y\mathcal{T}$, chiral, $\mathcal{PT}$ [49], anti-$\mathcal{PT}$, and reciprocity $\mathcal{R}$.

The energy spectrum of $H_{\rm NHW}(k)$ is $E_\pm^2(k) = a(k) \pm 2\sqrt{b(k)}$, where $a(k) = \sum_{i=1}^4 h_i^2 + m^2 - \delta^2$ and $b(k) = (h_2^2 + h_4^2)(m^2 - \delta^2) + 2ih_1h_2m\delta$. In Figs. 1(b) [Figs. 1(c) and 1(d)], we show the spectrum of $H_0(k)$ [$H_{\rm NHW}(k)$] as a function k_z, with a set of parameters, producing four Weyl nodes (eight EPs). We have confirmed numerically that the EPs are formed only at $k_x = 0$, and therefore from now on we work with this parameter with the highest number of EPs in the bulk. The location of these EPs as the function of k_z is obtained by solving the dispersion relation $E(k_z) = 0$, where k_x and k_y are fixed to be at zero. The eight EPs are located at values $\pm[\pi - \arccos(2\gamma + \delta + m' + 2)$, $\arccos(-2\gamma + \delta \pm m' - 2)$, and $\arccos(-2\gamma - \delta + m' - 2)]$ with $m' = \sqrt{2m^2 - \delta^2}$. For a fixed value of δ, when γ varies such that one goes from a phase with eight EPs to six EPS, two of the k_z values where EPs appear become complex (the argument of the arccos have a value greater than 1). Similar behavior has been observed whenever we cross the phase boundaries in Fig. 2. Their number clearly depends on γ and δ as m is kept constant. At $k_z = \pm\pi$, EPs annihilate each other to change their number. So we solve the dispersion relation at $k_z = \pm\pi$ to obtain the phase-space trajectory. Solving the dispersion relation of $H_{\rm NHW}(k)$ at $k_z = \pm\pi$, we get phase separation trajectory $(1 + 2\gamma \pm \delta)^2 = 2m^2 - \delta^2$. We evaluate the value of δ from the phase-space trajectory as

$$\left\{\delta \to \pm\tfrac{1}{2}\left[2\gamma \pm \sqrt{4m^2 - (2\gamma+1)^2} + 1\right]\right\}. \qquad (2)$$

For a fixed value of m, δ depends only on γ, and therefore we obtain two intersecting ellipses in the (γ-δ) plane, see Fig. 2. Notably, there exists a peculiar point in the parameter space $\gamma = -0.5$ and $\delta \sim 0.4$ where an infinitesimal change in the value of δ or γ will take to phases with different number of EPs therefore we coin it as triple point of EPs.

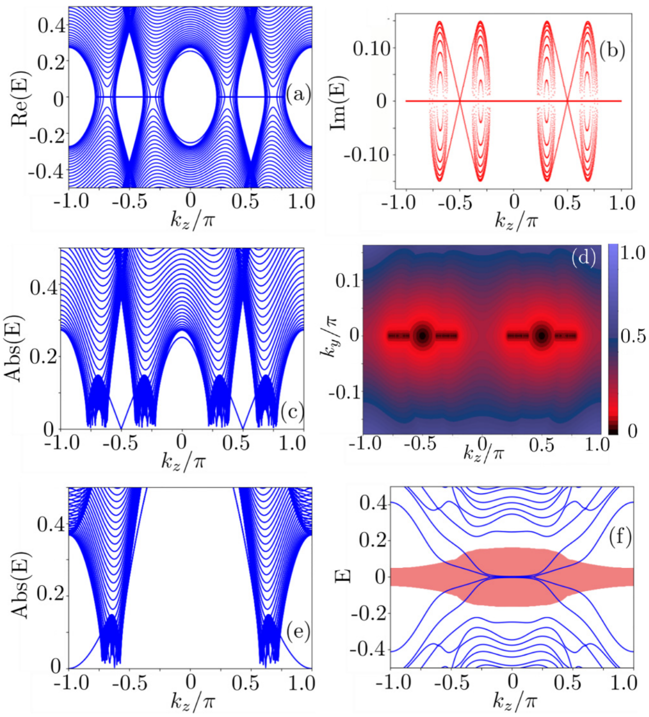

FIG. 3. (a) Real part of energy spectrum of $H_{\rm NHW}$ for x surface (at $k_y = 0$) as a function of k_z with same parameters as in Fig. 1. Of eight EPs four are connected by surface Fermi arcs, thus identifying them as normal-order EPs. The remaining four are connected through bulk Fermi arcs. (b) The corresponding imaginary part of the energy spectrum, forming a ringlike structure connecting EPs. Absolute energy spectrum for the x surface (c) demonstrating the formation of DPs at $k_z = \pm\pi/2$ and $k_y = 0$ with linear momenta dependency and (d) contour plot in (k_y-k_z) plane shows the formation of two Dirac cones around $(k_y, k_z) = (0, \pm\pi/2)$. The concentric circles are projections of Dirac cones. (e) Absolute energy eigenspectrum for $\gamma = -0.5$, having a dispersion with quadratic momenta dependency at BZ boundary. Therefore, behaving like a Luttinger phase on the surface of NHHOWS. (f) Finally, the real (blue) and imaginary (red) part of the energy spectrum for hinge states formed when we have open boundary condition (OBC) along the x and y directions. It clearly shows that innermost EPs close to $k_z = 0$ are connected through hinge states and therefore are named higher-order EPs. We have verified our results for different values of γ as well, see Appendix D.

III. SURFACE AND HINGE ANALYSIS

Further, we explore surface states by considering a tight-binding Hamiltonian along the x axis; for more details on tight-binding Hamiltonians, see Appendix A. In Fig. 3(a), we label the EPs from the extreme left; the EPs are connected via bulk FAs from positions 1 to 2, 3 to 4, 5 to 6, and 7 to 8 but from positions 2 to 3 and 6 to 7 via surface FAs. We call these EPs normal order as they are only connected through the surface states. Also as shown in Fig. 3(b), the imaginary part of the spectrum exhibits a ringlike structure connecting the EPs. Contrary to previous studies of NHWSM, the absolute value of E reveals that these Fermi arcs are dispersive in nature, see Figs. 3(c), 3(d) and 3(e). Without loss of generality, to simplify the analytical calculation, we consider $m = 2\,\delta$ throughout the paper. Next we provide an analytical solution to find the exact momenta values at which the DPs are formed. In principle, one should work with the slab Hamiltonian; however, with $H_{\rm slab}$ the analytical solution remains infeasible. Therefore, to proceed further, we project the bulk Hamiltonian along $k_x = 0$ and $k_y = 0$ momenta axes,

$$\begin{aligned} H(k_{z0}, \gamma, \delta, m) = {} & \left(\tfrac{1}{2}\cos k_{z0} + \gamma + 1\right)(\Gamma_4 + \Gamma_2) \\ & + im\sigma_0\kappa_1 + i\delta\sigma_0\kappa_2. \end{aligned} \tag{3}$$

To reduce one more variable we take $m = 2\delta$. The characteristics polynomial of the above projected Hamiltonian is given by the form,

$$E^4 + A\,E^2 + B = 0, \tag{4}$$

where E is the energy eigenvalue, A and B have the following forms:

$$\begin{aligned} A = {} & [\delta^2 - 2\gamma(\gamma+2)] - 8\delta^2 - \cos(k_{z0})[4\gamma + \cos(k_z) + 4] \\ & - 4, \end{aligned} \tag{5}$$

and

$$\begin{aligned} B = {} & -16\gamma(\gamma+2)\delta^2 + 4\gamma(\gamma+2)[\gamma(\gamma+2)+2] \\ & + 9\delta^4 - 16\delta^2 - 4\delta^2\cos(k_z)[4\gamma + \cos(k_z) + 4] \\ & + \tfrac{1}{4}\cos^2(k_z)[4\gamma + \cos(k_z) + 4]^2 \\ & + 2(\gamma+1)^2\cos(k_z)[4\gamma + \cos(k_z) + 4] + 4. \end{aligned} \tag{6}$$

We solve the characteristics polynomial for low energy, which is satisfied at $B/A = 0$. Also after neglecting the second- and third-order terms in δ, B/A further simplifies into

$$B/A = -\gamma(\gamma+2) - \tfrac{1}{4}\cos(k_z)[4\gamma + \cos(k_z) + 4] - 1 = 0, \tag{7}$$

which leads us to the following values of k_{z0}:

$$k_{z0} = \pm\cos^{-1}[-2(\gamma+1)]. \tag{8}$$

We note that k_{z0} is independent of m and δ and explicitly depends only on γ. Also, the DPs appear exactly at those locations where the Dirac nodes are formed in the HODS [26] phase; we also show using Schur's determinant identity that the eigenvalues corresponding to DPs are zero, see Appendix B. From this, one can clearly deduce that DPs retain the memory of HODS phase. The value of k_z matches exactly with the numerically obtained $k_{z0} = \pm\pi/2\,(0)$ for $\gamma = -1\,(-0.5)$. The distance between the two DPs increases (decreases) with the corresponding change in γ. At $k_{z0} = \pm\pi/2$, the functional form of absolute energy for the surface state is $\propto |k_z|$. Hence the surface of non-Hermitian higher-order Weyl semimetal (NHHOWS) is in the Dirac phase, hosting two Dirac cones at $k_{z0} = \pm\pi/2$. Interestingly at a particular value of $\gamma = -0.5$ these DPs merge at BZ boundary $k_z = \pm\pi$, having absolute energy dispersion as $\propto k_z^2$; see Appendix C. This kind of low energy dispersion along k_z resembles a quadratic Luttinger spectrum at BZ boundary [50–52]. Therefore, by tuning γ, we switch from Dirac to the Luttinger phase on the surface of NHHOWS. Further increasing γ above -0.5, the DPs completely merge, thus gapping out the energy spectrum. Also, we have analytically as well as numerically obtained that with the variation of γ, the dispersion is always linear along k_y and becomes nonlinear only along the k_z direction.

The contour plot of surface states in Fig. 3(d) reveals the fact that surface states are actually a collection of FAs, and as a result, they form conelike structures in the (k_y-k_z) plane.

Next, we explore the hinges of the system by applying OBC along the x and y directions [see Appendix D]. We observe that two innermost EPs closest to $k_z = 0$ are connected by hinge states, see Fig. 3(f). Therefore, we identify them as higher-order EPs. This phase is characterized by a topological invariant named the quadruple moment q_{xy} [46], which we will discuss in the next section. The absolute energy band diagram for hinge states confirms that, unlike surface FAs, these are perfectly flat bands connecting innermost EPs. The degeneracy of hinge states is four and in the Hermitian counterpart, each one of the states is localized at all of the corners of the (x-y) plane. However, for our NH system, these are localized in either two lower or two upper corners depending on whether we plot left $|\psi_L\rangle$ or right $|\psi_R\rangle$ wave functions; see Appendix D. We identify this fascinating effect as higher-order non-Hermitian skin effect (HONHSE). Moreover, we have explored models with different symmetry classes and discovered that the peculiar surface feature and the hinge state behavior remain unchanged. This illustrates the stability of the NHHOWS with surface DPs; for more information, see Appendix C.

IV. TOPOLOGICAL INVARIANTS

A. One-dimensional winding number

The Hamiltonian $H_{\mathrm{NHW}}(k)$ is not off-block diagonal for the chosen basis. So, in order to unravel the hidden sublattice symmetry of the model and make it an off-block diagonal, we change the basis by rotating the Pauli matrix (σ_s^i and κ_s^i) about the y axis. The transformations are as follows: $\sigma^x \to \kappa^y\sigma^x$, $\sigma^y \to \sigma^y$, $\sigma^z \to \kappa^y\sigma^z$ for σ_s^i and $\kappa^x \to \sigma^y\kappa^x$, $\kappa^y \to \kappa^y$, $\kappa^z \to \sigma^y\kappa^z$ for κ_s^i. After successfully applying these transformations to the Hamiltonian and projecting it along the x axis, the bulk Hamiltonian takes the form,

$$H_{\mathrm{NHW}}(k) = \begin{pmatrix} 0 & Q_1 \\ Q_2 & 0 \end{pmatrix}, \tag{9}$$

where the upper block is

$$Q_1 = (-im - \sin k_y)I_2 + i\left(\gamma + \delta + \cos k_y + \frac{\cos k_z}{2}\right)\sigma_y - i\left(\gamma + 1 + \frac{\cos k_z}{2}\right)\sigma_x, \tag{10}$$

and the lower block is

$$Q_2 = (im - \sin k_y)I_2 - i\left(\gamma - \delta + \cos k_y + \frac{\cos k_z}{2}\right)\sigma_y \times i\left(\gamma + 1 + \frac{\cos k_z}{2}\right)\sigma_x, \tag{11}$$

with the property $Q_2 \neq Q_1^\dagger$ for NH systems. The 1D winding number as a function of k_z is given by

$$W_{(1,2)}^{k_x=0}(k_z) = \int_{-\pi}^{\pi} \frac{1}{2\pi i}\partial_{k_y}\log(\det[Q_{1,2}(k_y, k_z)])dk_y. \tag{12}$$

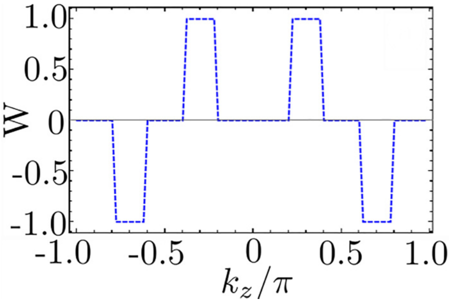

FIG. 4. Plot of one-dimensional winding number, $W = W_1 + W_2$, as a function of k_z with $k_x = 0$. It flips signs when it passes through EPs, highlighting their topological nature.

We notice that $W = W_1 + W_2$ flip sign after hitting any of the EPs and jumps from 0 to ±1, see Fig. 4. Therefore, we conclude that these bulk EPs are topological in nature.

B. Real-space open-boundary Chern number

In Hermitian systems, the appearance of robust topologically protected edge modes can be directly predicted only by looking at the bulk. These edge modes appear whenever there is a quantization of the Chern number or any of the topological indices in the bulk. So if one knows about the bulk, then the boundary can be predicted and vice versa; this well-known phenomenon is called BBC. This is a remarkable connection in Hermitian systems where the topological phase transition is marked by band touchings. On the contrary, NH systems do not follow the traditional BBC [41,44]. In such a scenario, it is quite difficult to reestablish a simplified correspondence between the bulk or boundary as in the case of Hermitian systems. Therefore, we calculate the topological invariant in real space with open boundaries as opposed to calculating them in momentum space. To begin with, we use the eigenstates of the Hamiltonian with OBC along two axes. For NH systems, one has right and left eigenstates satisfying the eigenvalue equation as $H\,|nR\rangle = E_n\,|nR\rangle$ and $H^\dagger\,|nL\rangle = E_n^*\,|nL\rangle$, respectively. The left and right eigenstates are chosen in such a way that the biorthonormality is maintained, $\langle mL|nR\rangle = \delta_{mn}$, $\langle mL|n'R\rangle = \langle m'L|nR\rangle = 0$. The primed states are the chiral partners of right (left) with negative eigenenergy $-E_n$ ($-E_n^*$). Furthermore, we compute the bulk band projection operator, $\hat{P}_\alpha = \sum_{n\in\alpha}|nR\rangle\langle nL|$. The sum is over all the unoccupied bands (labeled as α), i.e., below the Fermi level. Using $\hat{P}_\alpha$, the open-boundary Chern number is calculated as [45]

$$C_\alpha = \frac{2\pi\iota}{L_x'L_y'}Tr'(\hat{P}_\alpha[[\hat{X}, \hat{P}_\alpha], [\hat{Y}, \hat{P}_\alpha]]), \tag{13}$$

where $\hat{X}$ and $\hat{Y}$ are coordinate operators along the x and y axes for a 2D slice corresponding to each value of k_z, defined as $\hat{X}_{mm'} = x\delta_{mm'}$ and similarly for $\hat{Y}_{nn'} = y\delta_{nn'}$ with $1 \leqslant x \leqslant l_x$ ($1 \leqslant y \leqslant l_y$) where $l_x(l_y)$ is the size of the system along $x(y)$ with unit lattice spacing. Also $l'_{x/y}$ is defined as $l'_{x/y} = l_{x/y} - 2l_0$, where l_0 is a boundary layer that is being removed from $l_{x/y}$. After excluding the boundary layer only bulk information is captured by Tr' which is taken over the middle region. The open-boundary Chern number for each 2D k_z slice takes a quantized value, $C = -1$, exactly in the region

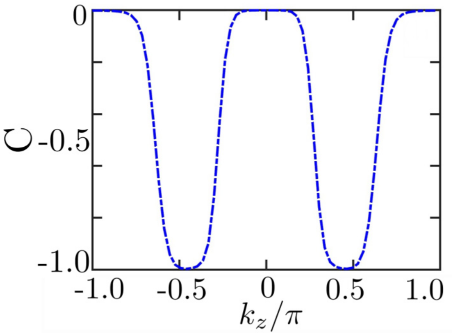

FIG. 5. The open-boundary Chern number has been plotted as a function of k_z, it takes an integer value of -1 only in the region where EPs are connected through surface states.

where surface states connecting the EPs appear; otherwise, its value is zero (see Fig. 5), thus reflecting the topological character of the collection of surface FAs. Therefore, this approach gives us a powerful tool for computing the Chern number in real space and successfully capturing the topological nature of the surface states.

C. Biorthogonal higher-order topological invariant: q_{xy}

It is well known that the appearance of hinge states is a clear signature of the higher-order topological phase of 3D systems [26,34]. Hinge gapless modes appear where the one-axis OBC spectrum (that is, the surface) is gapped. We notice that the innermost EPs closest to the Γ point in BZ are connected by fourfold degenerate hinge states. Thus, we conclude that the innermost EPs are higher order [37,38]. For Hermitian systems as well as their NH generalizations, higher-order topology can be characterized by the presence of a quadruple moment, q_{xy}. This kind of analysis is well explored in the existing literature [46,47] and is given by

$$Q_{\text{corner}} - p_x^{\text{edge}} - p_y^{\text{edge}} = -q_{xy}, \tag{14}$$

where p_x^{edge} (p_y^{edge}) is surface polarization along the $x(y)$ axis. The charge Q_{corner} is localized at the corners of each 2D k_z slice of the material. As mentioned in the previous section due to the presence of the NH skin effect and breaking down of BBC, it is challenging to use this formula [53] as the explicit calculations of p_x^{edge} and p_y^{edge} and corner charge(Q_{corner}) are complicated. In order to avoid all these complications and be motivated by the previous success of biorthogonal approach, we use a real-space operator-based formalism to calculate the quadruple moment q_{xy}. From a previous study [54], using the same line of thought q_{xy} is defined as

$$q_{xy} = \left[\frac{\operatorname{Im}(\ln[\det \hat{Q}]\,)}{2\pi} - \frac{\sum_i \hat{X}_i \hat{Y}_i}{2 l_x l_y}\right] \bmod 1, \tag{15}$$

where $\hat{Q}$ is a matrix whose elements are given by $\hat{Q}_{mn} = \langle mL| e^{\frac{2\pi i \hat{X}\hat{Y}}{l_x l_y}} |nR\rangle$ and $\hat{X}$ and $\hat{Y}$ are the same coordinate operators used to calculate Chern number in the previous section as well. For each 2D k_z slice from $[-\pi, \pi]$, we observe that q_{xy} takes quantized value of half where hinge states appear (connecting the innermost higher-order EPs); see Fig. 6.

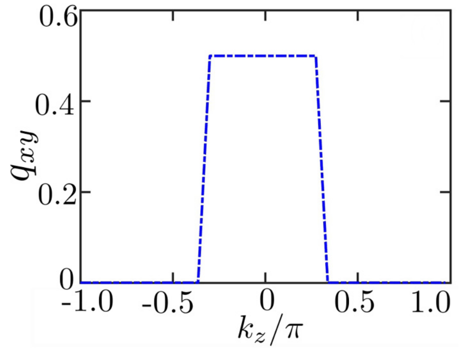

FIG. 6. Higher-order topological invariant quadruple moment q_{xy} is quantized to a value of half where hinge state connects the innermost EPs. The system parameters are the same as those used in Figs. 2(a)–2(d) and 2(f) for the Dirac phase. However, we have verified that all three invariants work perfectly for the Luttinger phase as well.

Therefore, again we are able to successfully characterize the higher-order topology of the hinge states.

V. MODEL PRESERVING INVERSION SYMMETRY

Here we present a model with explicit momentum dependence in the NH perturbation. As a result, it breaks the time-reversal symmetry ($\mathcal{T}$) but preserves inversion symmetry ($\mathcal{P}$) [55],

$$H_{\text{NHW}}^{\mathcal{I}}(k) = H_0(k) + i\,\delta\sigma_0\kappa_1 \sin k_z, \tag{16}$$

where $H_0(k)$ is the Hermitian part given as

$$H_0(k) = \sum_{j=1}^{4} h_j \Gamma_j + m\sigma_0\kappa_2. \tag{17}$$

Similarly to the previous model, here also we can control the number of EPs in the bulk. The EPs are either connected by first-order surface or higher-order hinge states, depending on the topological phase of the material. All the band diagrams corresponding to the bulk, surface, and hinges are plotted in Fig. 7. On increasing the value of γ, from -1.3 to -0.7, we are able to generate higher-order EPs in the bulk, which are connected by hinge states. Thus, one can traverse from a normal to a higher-order phase by tuning system parameters.

VI. MODEL PRESERVING TIME-REVERSAL SYMMETRY

Unlike the inversion symmetric model written in Eq. (16), here we introduce momentum dependence to the Weyl perturbation along with NH perturbation. Due to this change, the model breaks inversion symmetry ($\mathcal{P}$) but in turn preserves time-reversal symmetry ($\mathcal{T}$) with complex conjugate ($\mathcal{K}$) being the time-reversal operator,

$$H_{\text{NHW}}^{\mathcal{T}}(k) = H_0'(k) + i\,\delta\sigma_0\kappa_1 \sin k_z, \tag{18}$$

where $H_0'(k)$ is the Hermitian part with momentum-dependent Weyl perturbation,

$$H_0'(k) = \sum_{j=1}^{4} h_j \Gamma_j + m\sigma_0\kappa_2 \sin k_z. \tag{19}$$

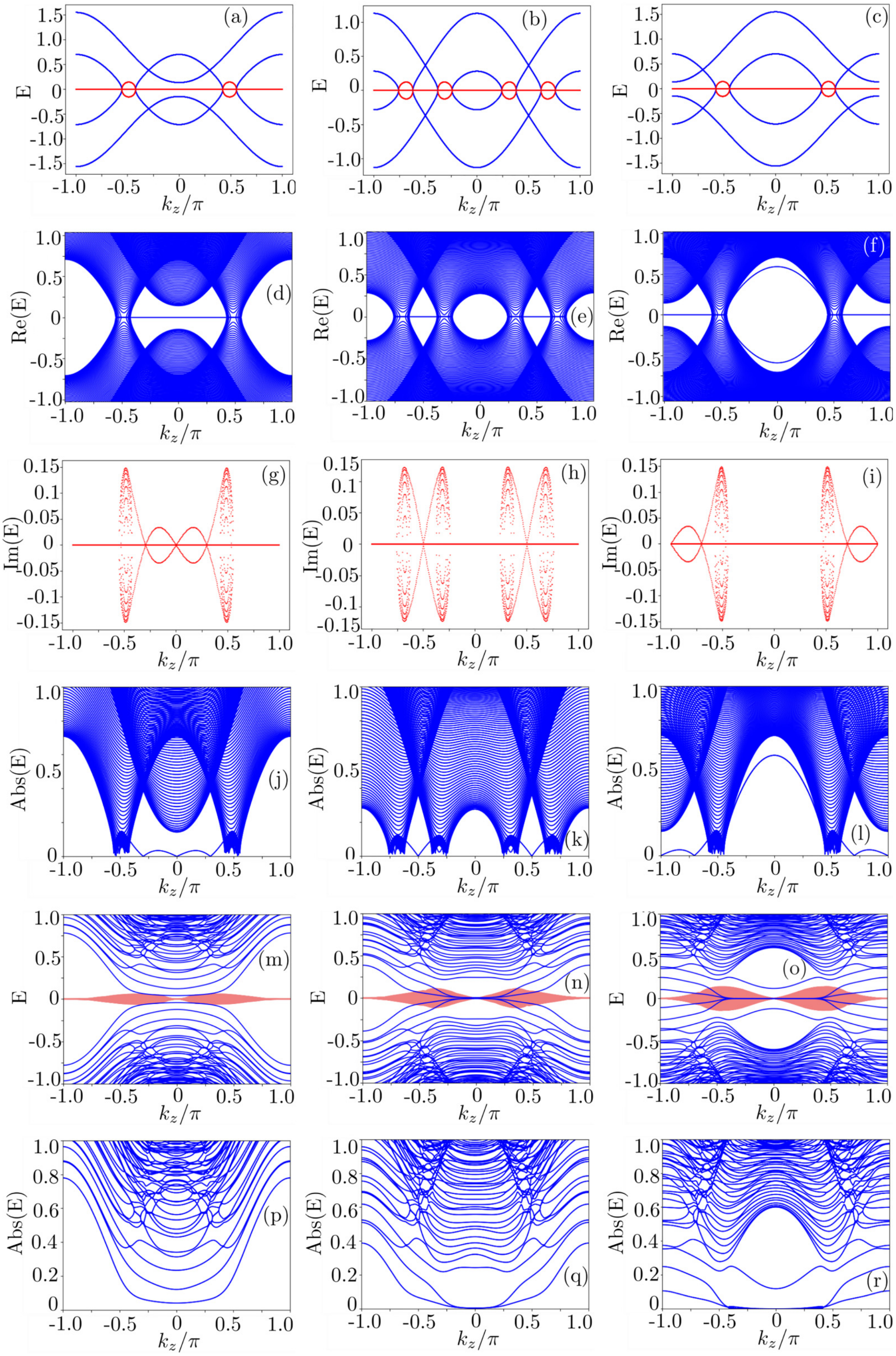

FIG. 7. [(a)–(c)] Bulk energy spectrum for inversion symmetric Hamiltonian written in Eq. (16), for $\gamma(-1.3, -1.0, -0.7)$ from left to the right column in all the rows. We consider m and δ to have the same values throughout. Corresponding real, imaginary, and absolute parts of eigenvalues for the x surface, have been shown in (d)–(f), (g)–(i), and (j)–(l), respectively. The absolute energy consists of DPs with modulating dispersion with the variation in γ. In (m)–(o), the real (blue) and imaginary (red) part of hinge spectrum with two-axes OBC for inversion symmetric model have been plotted. [(p)–(r)] Corresponding absolute energy spectrum for hinge states. Notably, the spectrum is linear close to DPs at $\gamma = -1$.

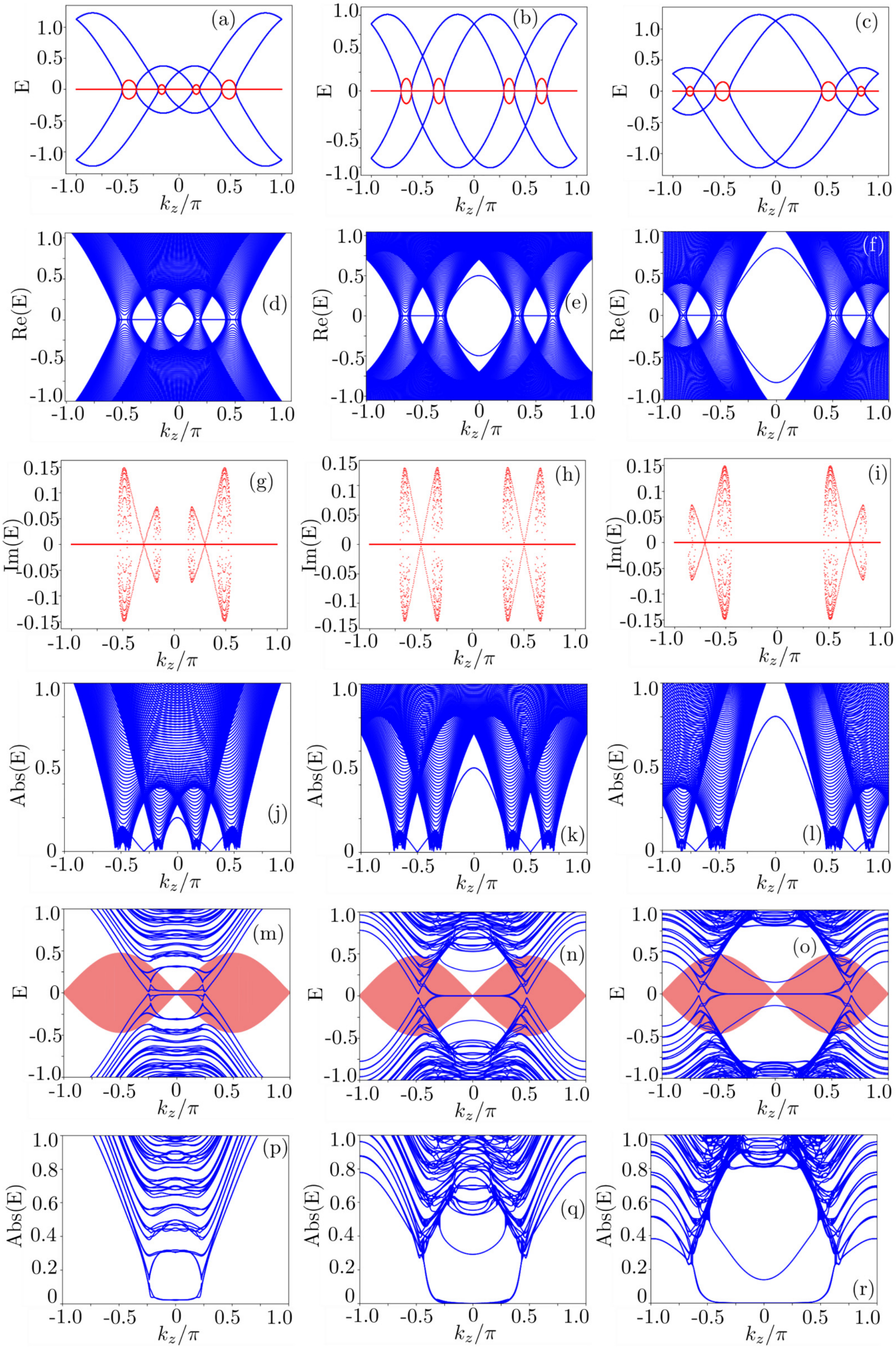

FIG. 8. [(a)–(c)] Bulk spectrum for the time-reversal symmetric model written in Eq. (18) for $\gamma = (-1.3, -1.0, -0.7)$. [(d)–(f)] Corresponding real eigenspectrum of x surface ($k_y = 0$) along k_z, showing surface FAs. [(g)–(i)] Imaginary eigenspectrum along k_z. [(j)–(l)] Same x surface but with absolute energy depicting DPs with modulating dispersion with change in γ. [(m)–(o)] Hinge spectrum with two-axis OBC for inversion symmetric model. [(p)–(r)] Corresponding hinge absolute energy spectrum. Other parameters are the same as used in Fig. 7.

The band diagrams of the TR symmetric model corresponding to the bulk, one-axis OBC surface, and two-axis OBC hinges are plotted in Fig. 8. In contrast to the inversion symmetric model, this model hosts eight EPs in the bulk for all three values of γ. We notice that of eight EPs, four are of the normal order in nature as they are connected by the surface states.

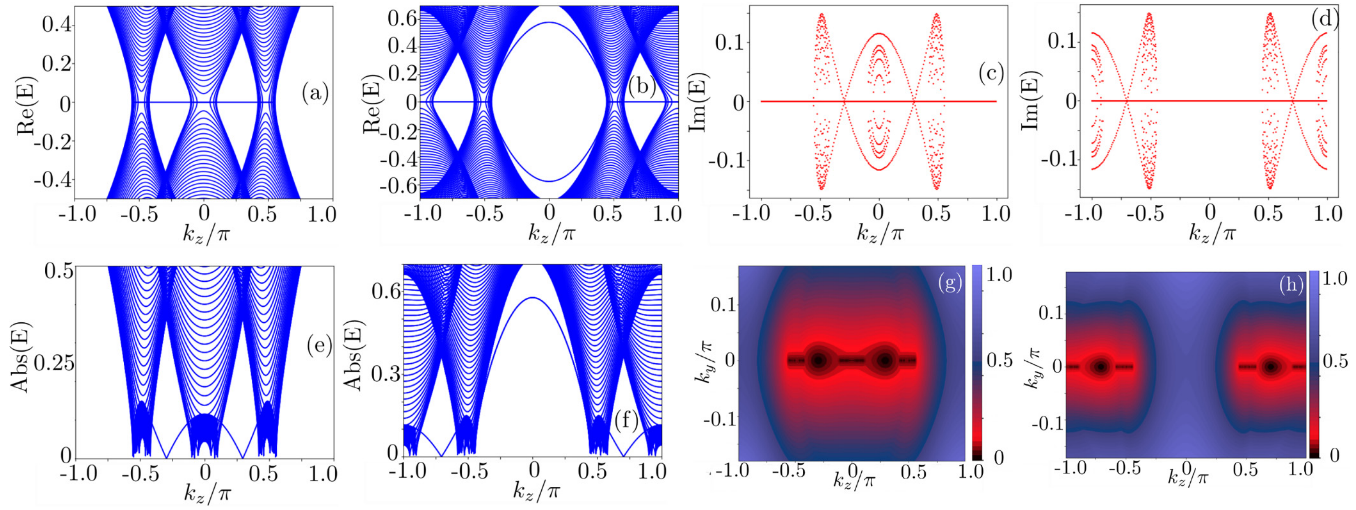

FIG. 9. Band diagrams for the slab Hamiltonian in Eq. (A1) as a function of k_z. (a) The real part of the energy spectrum for $\gamma = -1.3$. (b) Same plot for the parameter $\gamma = -0.7$. Both of them host zero-energy surface states. [(c) and (d)] Imaginary energy spectra for (a) and (b), respectively, both show the formation of concentric rings. [(e) and (f)] Plots of the absolute value of energy for $\gamma = -1.3$ and -0.7, respectively; one can clearly point out the deviation of dispersion around DPs from linear Dirac nature ($\gamma = -1.0$). [(g) and (h)] Contour plots for (e) and (f) respectively, in the (k_y-k_z) plane. These plots capture the nonlinear nature of the dispersion around the DPs (elliptical contour), which appear at $k_y = 0$ and $k_z = \cos^{-1}[-2(1+\gamma)]$.

At $\gamma = -1.3$, hinge states do not appear, and thus higher-order EPs are not present. As we vary γ, two EPs closest to $k_z = 0$ transform into higher order and are connected by fourfold degenerate hinge states, along with the remaining four first-order EPs. Figures 7 and 8 highlight the fact that there is no significant deviation in the outcome from the model discussed in Sec. II. This implies that these symmetries ($\mathcal{I}$ and $\mathcal{T}$) turn out to be futile for the model. Another interesting point is that the momenta values of DP and the form of low energy dispersion around them do not change when we are at Dirac phase ($\gamma = -1$) or in the Luttinger phase ($\gamma = -0.5$) even after invoking the above symmetries. We therefore conclude that the DPs on the surface do not require these symmetries to stabilize them.

VII. CONCLUSIONS

In summary, we have examined non-Hermitian HOWS and shown that the NH term provides us a potent tool to annihilate or create new EPs in the bulk of a system. Some of the EPs are connected through surface (hinge) states and are of normal order (higher order). We identify this new type of topological semimetal as NHHOWS with surface diabolic points. The surface of such a semimetal features some exotic phases like Dirac and Luttinger with linear and quadratic dispersion, respectively. This allows Dirac to Luttinger phase switching on the surface of NHHOWS as a function of system parameters. Additionally, we describe the topological properties of the EPs by first computing a 1D winding number and then implementing the biorthogonal method to obtain the open-boundary Chern number and q_{xy}. The latter two invariants identify the system's topological region, where surface and hinge states appear. The Chern number has an integer value of -1 and q_{xy} takes quantized value of half. Moreover, the biorthogonal technique stands out to be an essential tool in the context of computing topological invariants and subsequently capturing normal as well as higher-order topological phases of this system in a more versatile manner.

ACKNOWLEDGMENTS

For financial support, S.B. thanks CSIR (India) and M.T. thanks Science and Engineering Research Board (India) Grant No. SRG/2022/001408 and Young Faculty Incentive Fellowship from IIT Delhi. The authors thank F. Song for stimulating discussions on related topics.

APPENDIX A: SURFACE STATES ANALYSIS

In this section, we calculate the tight-binding Hamiltonian of $H_{\mathrm{NHW}}(k)$ with one axis OBC while maintaining PBC in the other two directions. The lattice version of the bulk Hamiltonian has the following form:

$$H_{\mathrm{slab}} = H_0 \sum_{x=1}^{N} c_x^\dagger c_x + \sum_{x=1}^{N-1} (t_x\, c_x^\dagger c_{x+1} + \mathrm{H.c.}), \tag{A1}$$

where $H_0(k_z, k_y, \gamma, \delta, m) = (\gamma + \frac{1}{2}\cos k_z)\Gamma_4 + (\gamma + \frac{1}{2}\cos k_z + \cos k_y)\Gamma_2 + \sin k_y \Gamma_1 + m\sigma_0\kappa_2$. and $t_x = \frac{1}{2}\Gamma_4 - i\Gamma_3$ and j is the unit cell index, we remind the readers that each unit cell has four spinless orbitals. The matrix form or the slab Hamiltonian of the above model is expressed in block off-diagonal form as

$$H_{\text{slab}} = \begin{bmatrix} H_0 & t_x & 0 & \dots & 0 & 0 & 0 \\ t_x^\dagger & H_0 & t_x & \dots & 0 & 0 & 0 \\ 0 & t_x^\dagger & H_0 & \dots & 0 & 0 & 0 \\ \vdots & \vdots & \vdots & \ddots & \vdots & \vdots & \vdots \\ 0 & 0 & 0 & \dots & H_0 & t_x & 0 \\ 0 & 0 & 0 & \dots & t_x^\dagger & H_0 & t_x \\ [3pt]0 & 0 & 0 & \dots & 0 & t_x^\dagger & H_0 \end{bmatrix}. \tag{A2}$$

The diagonal or the onsite part of the slab Hamiltonian is

$$\begin{aligned} &H_0(k_z, k_y, \gamma, \delta, m) \\ &\quad = \sin k_y\Gamma_1 + \left(\gamma + \tfrac{1}{2}\cos k_z + \cos k_y\right)\Gamma_2 \\ &\qquad + \left(\gamma + \tfrac{1}{2}\cos k_z\right)\Gamma_4 + (m\sigma_0\kappa_2 + i\delta\sigma_0\kappa_1), \end{aligned} \tag{A3}$$

whereas the off-diagonal part is

$$t_x = \begin{pmatrix} 0 & 0 & 1 & 0 \\ 0 & 0 & 0 & 0 \\ 0 & 0 & 0 & 0 \\ 0 & 1 & 0 & 0 \end{pmatrix} \quad \text{and} \quad t_x^\dagger = \begin{pmatrix} 0 & 0 & 0 & 0 \\ 0 & 0 & 0 & 1 \\ 1 & 0 & 0 & 0 \\ 0 & 0 & 0 & 0 \end{pmatrix}. \tag{A4}$$

The surface plots for the other two parameters, apart from $\gamma = -1$, are shown in Fig. 9.

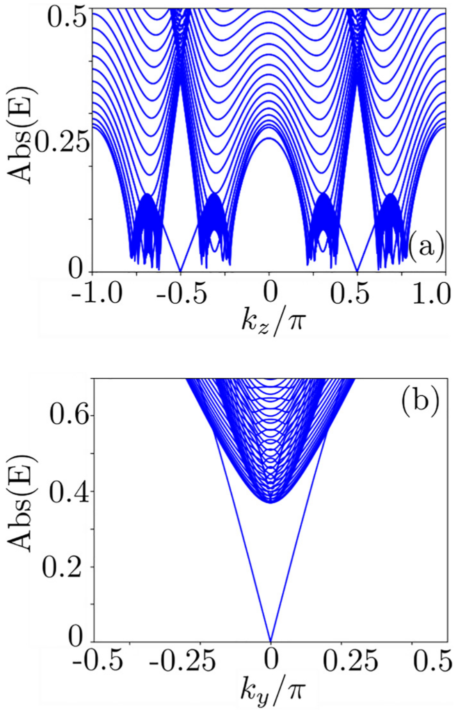

FIG. 11. Absolute energy band diagram for the OBC (surface) Hamiltonian of Sec. II (a) along k_z ($k_y = 0$) showing the formation of two Dirac cones with linear dispersion at low energy. These are formed exactly at $k_z = \pm\pi/2$. (b) Surface band diagram with same parameters along k_y ($k_z = \pm\pi/2$), depicting a single Dirac cone at $k_y = 0$. At this particular parameter, that is, $\gamma = -1$, low energy dispersion relations are linear along both the momenta direction.

APPENDIX B: SLAB CALCULATION FOR DIABOLIC POINTS: AN ANALYTICAL WAY TO MATCH EIGENVALUES

In this section, we provide an analytical way of calculating eigenvalues corresponding to DPs and their degeneracy. We begin by using the slab Hamiltonian [56] in Eq. (A1),

$$H_{\text{slab}} = \begin{bmatrix} H_0 & t_x & 0 & \dots & 0 & 0 & 0 \\ t_x^\dagger & H_0 & t_x & \dots & 0 & 0 & 0 \\ 0 & t_x^\dagger & H_0 & \dots & 0 & 0 & 0 \\ \vdots & \vdots & \vdots & \ddots & \vdots & \vdots & \vdots \\ 0 & 0 & 0 & \dots & H_0 & t_x & 0 \\ 0 & 0 & 0 & \dots & t_x^\dagger & H_0 & t_x \\ 0 & 0 & 0 & \dots & 0 & t_x^\dagger & H_0 \end{bmatrix}. \tag{B1}$$

In the diagonal or onsite part of the above Hamiltonian, we make the following substitutions: $k_z = \pi/2$, $k_y = 0$, $\gamma = -1$, and $m = 2\delta$. After substituting and simplifying it looks like

$$H_0(k_z = \pi/2, k_y = 0, \gamma = -1, \delta, m = 2\delta)$$

$$= \begin{pmatrix} 0 & -i\delta & -1 & 0 \\ 3i\delta & 0 & 0 & -1 \\ -1 & 0 & 0 & -i\delta \\ 0 & -1 & 3i\delta & 0 \end{pmatrix}. \tag{B2}$$

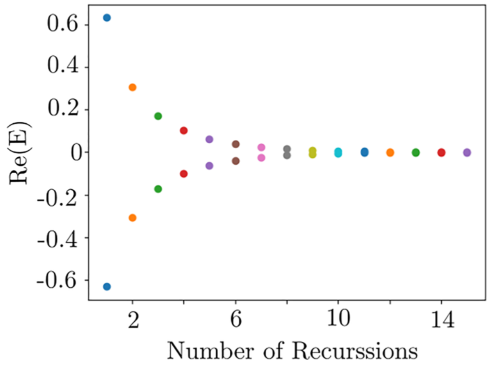

FIG. 10. Two lowest energy eigenvalues as a function of the number of times Schur's determinant identity is used. We recursively use this identity and show that with the increase in the lattice size these two eigenvalues ultimately converge to zero. This captures the degeneracy of the DPs as well as the finite-size effect of the system.

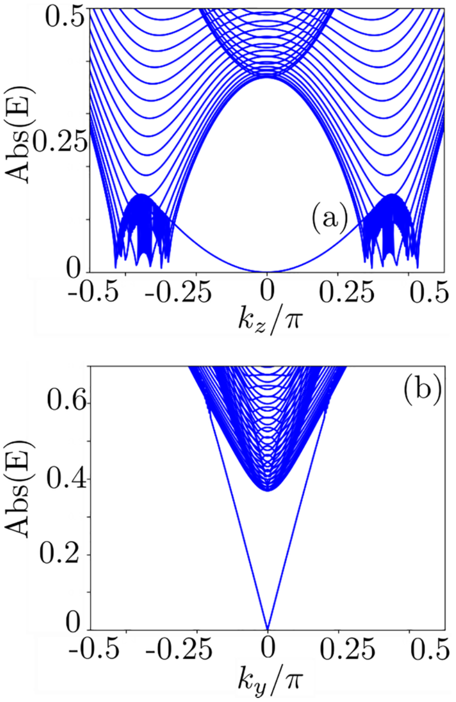

FIG. 12. Surface band diagram similar to Fig. 11 with $\gamma = -1.5$. (a) as a function of k_z ($k_y = 0$) depicting a Luttinger quadratic dispersion relation. At $\gamma = -0.5$ this quadratic dispersion is formed at $k_z = \pm\pi/2$ as shown in Fig. 2(e). (b) In the band diagram, a single Dirac cone has been observed as a function of k_y. Therefore, along k_y the dispersion is always linear in nature.

To derive the spectrum for these parameters, we analyze the solution of characteristics polynomial of $\det[H_{\text{slab}} - \lambda\mathbb{I}_{4N\times 4N}] = 0$ where square lattice size is $4N \times 4N$. Even after these simplifications, the analytical solution remains infeasible. Therefore, to tackle this problem, we use Schur's determinant identity [57],

$$\det\begin{pmatrix} A & B \\ C & D \end{pmatrix} = \det(D)\det(A - BD^{-1}C). \tag{B3}$$

We apply Schur's determinant identity in an iterative manner and obtain a recursion relation that allows us to calculate all eigenvalues. Final expression has the form $\det[H_{\text{slab}} - \lambda\mathbb{I}_{4N\times 4N}] = \prod_{j=1}^{N} \det a_j$ where $a_1 = H_0 - \lambda\mathbb{I}_{4X4}$ and $a_j = a_1 - t_x a_{j-1}^{-1} t_x^{\dagger}$ for $j \geqslant 2$. Finally, we take $\prod_{j=1}^{N} \det a_j = 0$ which gives us the eigenspectrum. We notice that there are two eigenvalues that converge to zero after continuing a series of iterations. The plot of the lowest energy solution with the number of times Schur's identity is being used has been shown in Fig. 10 with $\delta = 0.2$ in (B2). Ultimately these two values converge to zero, corresponding to a twofold degeneracy of DPs. It also captures the finite-size effect, which demands the lattice to be large enough such that the DPs are exactly at zero energy.

APPENDIX C: VERIFICATION OF LOW-ENERGY DISPERSION RELATION NEAR DIABOLIC POINTS

We notice that the DPs are formed on the x surface of the system. Therefore, we project the bulk Hamiltonian in the (k_y-k_z) plane, assuming $k_x = 0$. In principle, one should work with the slab Hamiltonian; however, with H_{slab} the analytical solution remains infeasible. Therefore, we work only with H_0 (the diagonal part which depends on momentas) to extract the dependency of E on k_y and k_z. First, we expand the Hamiltonian near these momenta values of DPs for small values of k_y which gives $e^{\pm ik_y} = 1 \pm ik_y$. Second, expansion of k_z around $\pm\pi/2$ gives $\cos(k_z) = \cos(k_z \pm \pi/2) = \pm\sin(k_z) = k_z$. This step tremendously simplifies the Hamiltonian, and thus the matrix form of H_0 takes the form

$$H_0(k_x = 0, k_z, k_y, \gamma = -1, \delta, m = \delta/2) = \begin{pmatrix} 0 & -i\delta & \frac{k_z}{2} & ik_y + \frac{k_z}{2} \\ 3i\delta & 0 & ik_y - \frac{k_z}{2} & \frac{k_z}{2} \\ \frac{k_z}{2} & -ik_y - \frac{k_z}{2} & 0 & -i\delta \\ -ik_y + \frac{k_z}{2} & \frac{k_z}{2} & 3i\delta & 0 \end{pmatrix}. \tag{C1}$$

Although this form of Hamiltonian looks simple, the analytical form of the eigenvalues is complicated. In order to reduce the complicated form of eigenvalues, we take $k_y = 0$ and solve the dispersion relation for k_z and vice versa. First taking $k_y = 0$, the dispersion relation along k_z has the form

$$E^4(k_z) = \left(k_z^2 + 2\sqrt{7}\delta k_z + 6\,\delta^2\right)\left(k_z^2 - 2\sqrt{7}\delta k_z + 6\,\delta^2\right)/4 = \left[\left(k_z^2 + 6\,\delta^2\right)^2 - 28\delta^2 k_z^2\right]/4 \tag{C2}$$

and, for $k_z = 0$, along k_y the dispersion takes the form

$$E^4(k_y) = (k_y - 3i\,\delta)(k_y + i\,\delta)(k_y + 3i\,\delta)(k_y - i\,\delta) = \left(k_y^2 + 9\delta^2\right)\left(k_y^2 + \delta^2\right). \tag{C3}$$

For small δ, along both axes dispersion of the absolute value of energy $\sim|k|$ is shown in Fig. 11. Therefore, we verify analytically the linear form of low energy dispersion along k_y and k_z direction around the DPs at $\gamma = -1$. On plotting the surface band diagrams, we notice that at $\gamma = -1.5$ or -0.5, the low energy dispersion around DPs is quadratic in nature along k_z and linear along k_y. This kind of quadratic dispersion is seen in Luttinger semimetals [50–52]. To analytically capture the quadratic dependency, we take $k_x = 0$ and expand close to $k_y, k_z \to 0$ such that $e^{\pm ik_y} = 1 \pm ik_y$ and $\cos(k_z) = 1 + \frac{k_z^2}{2}$ after neglecting higher-order terms. We note that the only difference between $\gamma = -1.5$ and -0.5 is the value of k_{z0}. Further, some algebraic

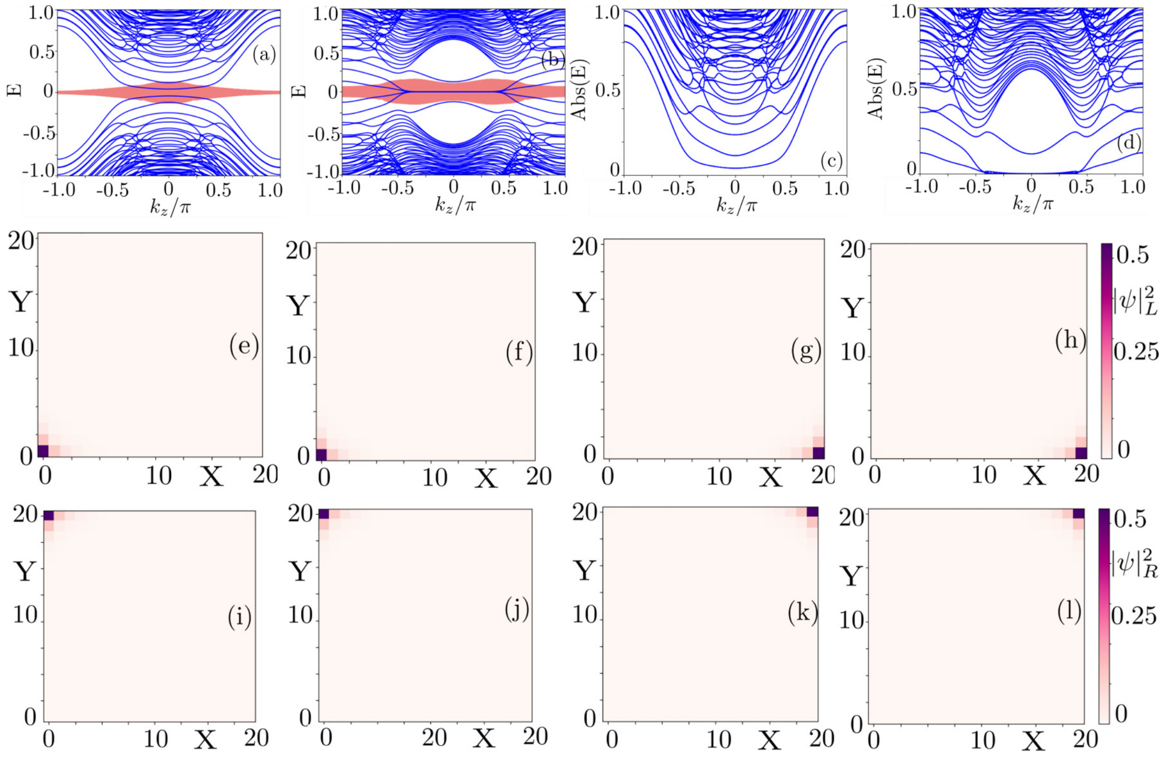

FIG. 13. The real (blue) and the imaginary (red) part of the energy eigenspectrum for a two-axis OBC Hamiltonian for (a) $\gamma = -1.3$ and (b) $\gamma = -0.7$ as a function of k_z. In (b) hinge states appear connecting two EPs (higher order) and therefore, for this parameter value, H_{NHW} is in the higher-order topological phase [(c) and (d)] corresponding to the absolute energy plots for (a) and (b). [(e)–(h)] Plot of the left-handed wave function $|\psi_L\rangle$ of four fold degenerate hinge states evaluated at $k_z = 0$ and $\gamma = -0.7$. Out of four, there are two distinct-looking wave functions forced to be caged at the lower two corners because of HONHSE. [(i)–(l)] The corresponding right wave function $|\psi_R\rangle$ evaluated in same region for the same parameter value. Remarkably, these are localized at the upper two corners.

manipulations simplify the Hamiltonian into

$$H_0(k_x = 0, k_y, k_z, \gamma = -1.5, \delta, m = \delta/2) = \begin{pmatrix} 0 & -i\delta & \frac{k_z^2}{4} & ik_y + \frac{k_z^2}{4} \\ 3i\delta & 0 & ik_y - \frac{k_z^2}{4} & \frac{k_z^2}{4} \\ \frac{k_z^2}{4} & -ik_y - \frac{k_z^2}{4} & 0 & -i\delta \\ -ik_y + \frac{k_z^2}{4} & \frac{k_z^2}{4} & 3i\delta & 0 \end{pmatrix}. \tag{C4}$$

It has an exactly similar form to Eq. (C1) where only $k_z/2$ gets replaced with $k_z^2/4$ and remarkably ik_y remains the same. Therefore, using a similar analysis we can account for quadratic dispersion, with an absolute value of $E \sim k_z^2$ along one axis and k_y along another. This kind of dispersion relation is captured in Fig. 12.

APPENDIX D: HINGE STATE ANALYSIS

In order to construct the hinges of the bulk system, we apply OBC along the x and y axes; however, PBC is maintained along the z direction. The lattice Hamiltonian in two directions takes the form

$$H_{\text{hinge}} = H_0 \sum_{x,y=1,1}^{N_x,N_y} c^\dagger_{x,y} c_{x,y}\ \delta_{x,y} + \left(t_x \sum_{x,y=1,1}^{N_x-1,N_y} c^\dagger_{x,y} c_{x+1,y} + t_y \sum_{x,y=1,1}^{N_x,N_y-1} c^\dagger_{x,y} c_{x,y+1} + \text{H.c.} \right), \tag{D1}$$

where $N_x = N_y = N$ is the number of unit cells along the x and y directions on a square lattice. The form of H_0 has the following form:

$$H_0(k_z, \gamma, \delta, m) = \begin{pmatrix} 0 & i\delta - im & \gamma + \frac{\cos k_z}{2} & \gamma + \frac{\cos k_z}{2} \\ i\delta + im & 0 & -\gamma - \frac{\cos k_z}{2} & \gamma + \frac{\cos k_z}{2} \\ \gamma + \frac{\cos k_z}{2} & -\gamma - \frac{\cos k_z}{2} & 0 & i\delta - im \\ \gamma + \frac{\cos k_z}{2} & \gamma + \frac{\cos k_z}{2} & i\delta + im & 0 \end{pmatrix}, \tag{D2}$$

and the hopping matrices are

$$t_x = \begin{pmatrix} 0 & 0 & 1 & 0 \\ 0 & 0 & 0 & 0 \\ 0 & 0 & 0 & 0 \\ 0 & 1 & 0 & 0 \end{pmatrix} \quad \text{and} \quad t_y = \begin{pmatrix} 0 & 0 & 0 & 1 \\ 0 & 0 & 0 & 0 \\ 0 & -1 & 0 & 0 \\ 0 & 0 & 0 & 0 \end{pmatrix}. \tag{D3}$$

The band diagram figure for the Hamiltonian H_{hinge} depicts that for $\gamma = -1.3$, the hinges are fully gapped; however, for $\gamma = -0.7$, hinge states connect the two EPs closest to $k_z = 0$. This marks the higher-order topological phase of H_{NHW}. We check that these hinge states are fourfold degenerate with absolute zero energy eigenvalues. The energy spectrum and eigenstates are shown in Fig. 13. Notably, the hinge states occupy only the lower corners. This mismatch is because this model possesses HONHSE [43], and, as a result, hinges are caged in the lower corners only. In order to visualize all four hinge localizations, we plot the left $|\psi_L\rangle$ along with right $|\psi_R\rangle$ wave functions.

[1] W. P. Su, J. R. Schrieffer, and A. J. Heeger, Phys. Rev. Lett. **42**, 1698 (1979).

[2] J. K. Asbóth, L. Oroszlány, and A. Pályi, *A Short Course on Topological Insulators* (Springer, Berlin, 2016), pp. 1–22.

[3] S. Bid and A. Chakrabarti, Phys. Lett. A **423**, 127816 (2022).

[4] F. Schindler, A. M. Cook, M. G. Vergniory, Z. Wang, S. S. P. Parkin, B. A. Bernevig, and T. Neupert, Sci. Adv. **4**, eaat0346 (2018).

[5] A. Udupa, K. Sengupta, and D. Sen, Phys. Rev. B **98**, 205413 (2018).

[6] M. Sato and Y. Ando, Rep. Prog. Phys. **80**, 076501 (2017).

[7] D. Sen and O. Deb, Phys. Rev. B **85**, 245402 (2012).

[8] A. K. Ghosh, T. Nag, and A. Saha, Phys. Rev. B **105**, 155406 (2022).

[9] M. Thakurathi, K. Sengupta, and D. Sen, Phys. Rev. B **89**, 235434 (2014).

[10] A. K. Ghosh and T. Nag, Phys. Rev. B **106**, L140303 (2022).

[11] M. Thakurathi, D. Chevallier, D. Loss, and J. Klinovaja, Phys. Rev. Res. **2**, 023197 (2020).

[12] K. Plekhanov, N. Müller, Y. Volpez, D. M. Kennes, H. Schoeller, D. Loss, and J. Klinovaja, Phys. Rev. B **103**, L041401 (2021).

[13] B. Pérez-González, M. Bello, Á. Gómez-León, and G. Platero, Phys. Rev. B **99**, 035146 (2019).

[14] A. Y. Kitaev, Phys. Usp. **44**, 131 (2001).

[15] C. Beenakker, Annu. Rev. Condens. Matter Phys. **4**, 113 (2013).

[16] M. Thakurathi, P. Simon, I. Mandal, J. Klinovaja, and D. Loss, Phys. Rev. B **97**, 045415 (2018).

[17] S. Hoffman, J. Klinovaja, and D. Loss, Phys. Rev. B **93**, 165418 (2016).

[18] A. A. Burkov and L. Balents, Phys. Rev. Lett. **107**, 127205 (2011).

[19] G. C. Paul, S. F. Islam, P. Dutta, and A. Saha, Phys. Rev. B **103**, 115306 (2021).

[20] A. A. Burkov, Phys. Rev. B **99**, 035124 (2019).

[21] D. Sehayek, M. Thakurathi, and A. A. Burkov, Phys. Rev. B **102**, 115159 (2020).

[22] M. Thakurathi and A. A. Burkov, Phys. Rev. B **101**, 235168 (2020).

[23] B. Roy, Phys. Rev. Res. **1**, 032048 (2019).

[24] G. K. Dash, S. Bid, and M. Thakurathi, arXiv:2301.13119 (2023).

[25] T. Liu, Y.-R. Zhang, Q. Ai, Z. Gong, K. Kawabata, M. Ueda, and F. Nori, Phys. Rev. Lett. **122**, 076801 (2019).

[26] S. A. A. Ghorashi, T. Li, and T. L. Hughes, Phys. Rev. Lett. **125**, 266804 (2020).

[27] H. Shen, B. Zhen, and L. Fu, Phys. Rev. Lett. **120**, 146402 (2018).

[28] Y. Ashida, Z. Gong, and M. Ueda, Adv. Phys. **69**, 249 (2020).

[29] A. A. Zyuzin and A. Y. Zyuzin, Phys. Rev. B **97**, 041203 (2018).

[30] E. J. Bergholtz and J. C. Budich, Phys. Rev. Res. **1**, 012003 (2019).

[31] A. Soori, M. Sivakumar, and V. Subrahmanyam, J. Phys.: Condens. Matter **35**, 055301 (2023).

[32] Y. Xu, S.-T. Wang, and L.-M. Duan, Phys. Rev. Lett. **118**, 045701 (2017).

[33] T. Liu, J. J. He, Z. Yang, and F. Nori, Phys. Rev. Lett. **127**, 196801 (2021).

[34] H.-X. Wang, Z.-K. Lin, B. Jiang, G.-Y. Guo, and J.-H. Jiang, Phys. Rev. Lett. **125**, 146401 (2020).

[35] M. Lin and T. L. Hughes, Phys. Rev. B **98**, 241103 (2018).

[36] H. Zhou, C. Peng, Y. Yoon, C. W. Hsu, K. A. Nelson, L. Fu, J. D. Joannopoulos, M. Soljačić, and B. Zhen, Science **359**, 1009 (2018).

[37] H. Hodaei, A. U. Hassan, S. Wittek, H. Garcia-Gracia, R. El-Ganainy, D. N. Christodoulides, and M. Khajavikhan, Nature (London) **548**, 187 (2017).

[38] I. Mandal and E. J. Bergholtz, Phys. Rev. Lett. **127**, 186601 (2021).

[39] S. Yao and Z. Wang, Phys. Rev. Lett. **121**, 086803 (2018).

[40] D. S. Borgnia, A. J. Kruchkov, and R.-J. Slager, Phys. Rev. Lett. **124**, 056802 (2020).

[41] N. Okuma, K. Kawabata, K. Shiozaki, and M. Sato, Phys. Rev. Lett. **124**, 086801 (2020).

[42] E. J. Bergholtz, J. C. Budich, and F. K. Kunst, Rev. Mod. Phys. **93**, 015005 (2021).

[43] X. Zhang, Y. Tian, J.-H. Jiang, M.-H. Lu, and Y.-F. Chen, Nat. Commun. **12**, 1 (2021).

[44] F. K. Kunst, E. Edvardsson, J. C. Budich, and E. J. Bergholtz, Phys. Rev. Lett. **121**, 026808 (2018).

[45] F. Song, S. Yao, and Z. Wang, Phys. Rev. Lett. **123**, 246801 (2019).

[46] W. A. Benalcazar, B. A. Bernevig, and T. L. Hughes, Phys. Rev. B **96**, 245115 (2017).

[47] W. A. Benalcazar, B. A. Bernevig, and T. L. Hughes, Science **357**, 61 (2017).

[48] D. Zou, T. Chen, W. He, J. Bao, C. H. Lee, H. Sun, and X. Zhang, Nat. Commun. **12**, 7201 (2021).

[49] R. El-Ganainy, K. G. Makris, M. Khajavikhan, Z. H. Musslimani, S. Rotter, and D. N. Christodoulides, Nat. Phys. **14**, 11 (2018).

[50] I. Boettcher and I. F. Herbut, Phys. Rev. B **93**, 205138 (2016).

[51] S. A. A. Ghorashi, P. Hosur, and C.-S. Ting, Phys. Rev. B **97**, 205402 (2018).

[52] I. Mandal and H. Freire, Phys. Rev. B **103**, 195116 (2021).

[53] S. A. A. Ghorashi, T. Li, M. Sato, and T. L. Hughes, Phys. Rev. B **104**, L161116 (2021).

[54] H. Wu, B.-Q. Wang, and J.-H. An, Phys. Rev. B **103**, L041115 (2021).

[55] T. L. Hughes, E. Prodan, and B. A. Bernevig, Phys. Rev. B **83**, 245132 (2011).

[56] M. M. Denner, A. Skurativska, F. Schindler, M. H. Fischer, R. Thomale, T. Bzdušek, and T. Neupert, Nat. Commun. **12**, 5681 (2021).

[57] F. Terrier and F. K. Kunst, Phys. Rev. Res. **2**, 023364 (2020).